Characterization of plasmon-resonant gold nanorods as near-infrared optical contrast agents investigated using a double-integrating sphere system

Amy Oldenburg[a], Daniel A. Zweifel[b], Chenyang Xu[a], Alexander Wei[b], and Stephen A. Boppart[a]

[a]Department of Electrical and Computer Engineering, Beckman Institute for Advanced Science and Technology, University of Illinois at Urbana-Champaign, 405 N. Mathews Ave., Urbana, IL 61801

[b]Department of Chemistry, Purdue University, 560 Oval Dr., West Lafayette, IN 47907

ABSTRACT

The potential for using plasmon-resonant gold nanorods as targeted contrast agents for *in vivo* coherent optical imaging is investigated. Separation of the relative strengths of light scattering and absorption of plasmon-resonant nanorods are measured with a double-integrating sphere system at 774 and 1304nm. The maximum likelihood ratio is then used to test the statistical significance of optical changes observed after application of contrast agents to tissue phantoms. Gold plasmon-resonant nanorods with a longitudinal resonance near 800nm are imaged within varying concentrations of intralipid using a 101dB sensitivity, 800nm optical coherence tomography (OCT) system. We estimate the minimum OCT detectible concentration of these nanorods (ca. 15×45nm) within 1.1% intralipid to be 25μg/mL of gold.

Keywords: Contrast agents, plasmon resonance, nanorods, optical coherence tomography, integrating spheres

1. INTRODUCTION

Minimally-invasive *in vivo* imaging is important from both a clinical, biomedical standpoint and also for small-animal researchers looking for investigational tools that do not disturb the living system under study. Near-infrared optical imaging is essentially non-invasive at moderate light intensities, but it suffers from a tradeoff between tissue penetration and resolution. This may be improved through the use of exogenous agents, which enhance the tissue contrast and furthermore highlight specific molecular events within the subject. In small animal optical imaging, bioluminescent[1] and other fluorescent agents have provided a wealth of new information on molecular events. However, as such agents rely on inelastic scattering, (*e.g.*, fluorescent processes), they can only be used with incoherent light imaging systems such as confocal or multiphoton microscopy and diffusion tomography. The advantage to coherence imaging is that the phase of the incident light is preserved which allows depth resolution through coherence gating, provides additional signal-to-noise ratios (SNR) via heterodyning, and reveals dynamic processes by speckle analysis.

The choice of plasmon-resonant gold nanoparticles as contrast agents for coherent light imaging is motivated by several factors: 1) the known biocompatibility of gold, 2) the small size of the nanoparticles, minimizing their invasiveness and increasing their portability in tissue, and 3) the high scattering efficiencies (>1) of these agents afforded at the nanoscale, unlike dielectrics which typically must be micron-sized to achieve efficiencies near unity. There is an important tradeoff between these latter two factors because in the Rayleigh regime ($D<<\lambda$), the scattering efficiency falls off as D^6 and absorption as D^3, where D is the diameter of the particle. With any potential *in vivo* contrast agent, the question one is obliged to answer is, can these agents be detected inside tissue at a concentration and particle size that is non-toxic, and ideally completely non-disruptive?

Surface plasmon resonance is known as the collective excitation of electrons occurring during the optical excitation of metal nanoparticles.[2] It has been shown that gold nanorods exhibit a linear relationship between their aspect ratio and the peak wavelength of their longitudinal resonance,[3] allowing wavelength tuning. In an aqueous

Plasmonics in Biology and Medicine II, edited by Tuan Vo-Dinh, Joseph R. Lakowicz, Zygmunt K. Gryczynski, Proceedings of SPIE Vol. 5703 (SPIE, Bellingham, WA, 2005) · 1605-7422/05/$15 · doi: 10.1117/12.589617

medium, this resonance is expected to reach 750-800nm (*i.e.*, within the optical window for biomedical imaging) when the rods exhibit aspect ratios between 3 and 4.[3] For optical sensing applications, it is interesting to consider the relative contributions of absorption and scattering to the total light extinction. Mie computations for gold spheres as a function of size[4] indicate a crossover from low albedo (absorption dominant) to high albedo (scattering dominant) particles at approximately 80nm. For nanorods of similar geometry to those studied here, measurements of the single-particle plasmon-resonant linewidth result in an estimation of the quantum efficiency of radiative decay to be 10%.[5] Others have observed that scattering begins to become significant for rod lengths >60nm.[6] In one paper[7] it has been suggested that for optically excited metal particles of arbitrary shape and nominally 100nm size, radiation will dominate over dissipation.

The use of single- and double-integrating spheres in conjunction with a radiative transfer model for separation of the relative contributions of absorption and scattering has proven to be a reliable metrological technique within optically dense media,[8] or even for backing out the refractive indices of monodisperse particles.[9] A double-integrating sphere apparatus is desirable in situations where the sample must be monitored during an external stimulus such as heating, or simply because it does not require additional movement of the sample or optical beam.

Here we investigate the optical properties of plasmon-resonant nanorods for the purposes of estimating the detectability of such agents via modification of the depth-dependent backscattering in OCT imaging. In related work, the *in vivo* detection of polystyrene spheres was investigated with confocal microscopy,[10] where a criterion for detectability is based upon the scattering amplitude of the agent and the SNR of the microscope. In OCT, the depth-dependent scattering has been modeled as a function of the scattering coefficient μ_s of the medium, resulting in good agreement between integrating sphere measurements and OCT images.[11] A careful noise analysis[12] of the ability to determine μ_s from OCT depth scans in various types of tissue has also been performed. However, these studies lack a treatment of the absorption coefficient μ_a (because it is typically much smaller than μ_s in tissue in the near infrared), which is significant in this work using plasmon-resonant particles. It should be noted that other promising techniques for producing contrast in OCT are currently under investigation, including the use of highly wavelength-dependent agents,[13] the *in situ* modification of contrast agent spectral properties[14] and the physical perturbation of magnetic agents.[15]

2. THEORY

Clearly, a figure of merit for any type of contrast agent is its minimum detectible concentration in tissue. However, in order for this to be meaningful, one must also weight this by the relative cytotoxicity of the agent in question. If one were to consider particles of a given chemistry but varying size, then a reasonable first approximation to the effect of cytotoxicity is that it is proportional to the fractional volume f of the particles. (One may choose to reference this to the particle number density N by $f=V_p$(particle volume)$\times N$. In our case, f is simpler to measure because it does not require precise knowledge of V_p, which would need to be averaged over the particle distribution). We therefore consider the primary figure of merit to be the minimum detectible f of contrast agents in tissue, which is specific to the agent chemistry and tissue type, and scales with the imaging system sensitivity and depth of imaging. In addition, the agent detectability depends on the area or volume over which the optical response can be averaged to achieve sufficient statistics. Ideally, one wishes to generate a concentration map corresponding to a pair of optical images acquired before (A) and after (A') introduction of the agents into tissue. For a given set of pixels a within A and a' within A' (which define our mapping resolution), the estimate of f is chosen by maximizing the likelihood ratio, which is the ratio of the probability of measuring a' given agents at f to the probability of measuring a' given no agents. In this way, the maximum likelihood ratio (MLR) is used to not only determine the best f, but to estimate the significance of this determination. We therefore use the MLR as a measure of the detectability of the agent. In practice we evaluate the natural log of the MLR as follows, where we assume all probabilities are governed by normal Gaussian distributions:

$$ln(MLR) = \frac{P(\textit{measurement consistent with agents at concentration } f)}{P(\textit{measurement consistent with no agents})}$$

$$= ln\left(\frac{\prod_{z_i} P(s(z_i) : \bar{s}(z_i, f), \sigma_f)}{\prod_{z_i} P(s(z_i) : \bar{s}(z_i, 0), \sigma_0)}\right) = \sum_{z_i}\left(\frac{(s(z_i) - \bar{s}(z_i, 0))^2}{2{\sigma_0}^2} - \frac{(s(z_i) - \bar{s}(z_i, f))^2}{2{\sigma_f}^2}\right) \quad (1)$$

where $s(z_i)$ is the OCT signal measured at depth z_i, and $\bar{s}(z_i, f)$ and σ_f are the predicted OCT signal and standard deviation given contrast agent concentration f.

The predicted depth dependence of the OCT signal is modeled by the following expression:

$$\begin{aligned}\bar{s}(z) &= s_0(\mu_s, g, NA)\exp\left(-\sum_i \mu_{t,i} \cdot f_i \cdot z\right)\exp\left(\left(-2(z - z_f)/b\right)^2\right) \\ &= s_0 \exp(-cz)\exp\left(-\left(2(z - z_f)/b\right)^2\right)\end{aligned} \tag{2}$$

where i here indicates each species within the medium contributing to the light extinction. We approximate the depth dependence of the OCT signal as an exponential decay due to light extinction $\mu_t = \mu_s + \mu_a$. A Gaussian correction factor accounting for increased backscattering at the lens focus at z_f (with confocal parameter b) is also necessary to achieve a good fit with the data; however, z_f and b can be measured once and utilized for all samples (it is sample-independent). The scattered light within the sample is only detected if it is collected by the imaging optics of numerical aperture NA, which is dependent on the average cosine of the scattering angle g. By least-squares fitting our measurements to Eq. 2 with the two parameters s_0 and c, we are effectively finding the concentrations of species f_i that maximize the likelihood ratio.

3. EXPERIMENT

3.1 Synthesis of Plasmon-Resonant Gold Nanorods

Gold nanorods were synthesized with a nominal aspect ratio of 4, using a seeded growth method mediated by $AgNO_3$ and hexadecyltrimethylammonium bromide (CTAB) as a surfactant.[16] Their extinction spectra exhibit a maximum near 800nm as expected[3] due to their longitudinal plasmon resonance. Three independently synthesized batches of nanorods were investigated. Representative TEMs of each batch are displayed in Fig. 1. As shown, the aspect ratios appear to range between 3-4, except in the second batch where some rods have reverted to a sphere-like shape of ~35nm diameter. The age of batch #2 is 1 year and the others are only 2-3 months old, suggesting a shelf life between 3 and 12 months. The long axes of the nanorods are 40-80nm. Gold microanalysis by acid digestion and subsequent inductively-coupled plasma mass spectrometry (OES Optima 2000 DV, Perkin Elmer) indicated 229.3, 130.7, and 33.8ppm Au (wt/vol) for batches 1, 2 and 3, respectively. It is important to note that the size and aspect ratios of the Au nanorods slowly change over time, but can be stabilized by treating the suspensions with sodium sulfide after synthesis.[17]

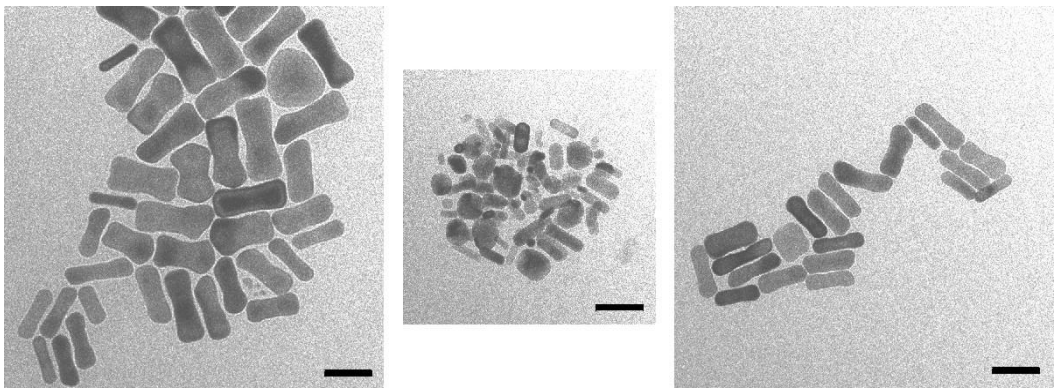

Figure 1: Transmission electron micrographs of gold plasmon-resonant nanorods shown at identical magnification, scale bar = 50nm. Left: Batch #1, Image size: 400×400nm. Middle: Batch #2, Image size: 300×300nm. Right: Batch #3, Image size: 400×400nm.

3.2 Double-Integrating Sphere Setup and Measurements

A custom double-integrating sphere system[18] was constructed to separate the relative contributions of absorption and scattering to the total light extinction within a sample. The choice of a double- over a single-integrating sphere system

is motivated by simplicity (not having to move the sample or beam to acquire reflection and transmission measurements) and by the ability to conduct future experiments by monitoring a state change in the sample in real-time. Two identical spheres (SphereOptics-Hoffman, LLC) of 50.8mm radius with an inner Lambertian coating (Zemax, reflectivity m(774nm)=0.9782, m(1304nm)=0.9757) were employed as shown in Fig. 2. The light sources consisted of collimated laser diodes centered at 773.5 and 1304.4nm, apertured slightly to beam diameters of 3mm and 2mm, and with powers incident on the sample of 1.64mW and 1.17mW, respectively. The collimated transmission T_c was measured with Coherent Field Master GS (774nm) and Coherent FieldMax (1304nm) power meters at a position 700mm from the sample. The backward- and forward-scattered light was collected by each sphere and diffusely reflected onto Si (774nm) and Ge (1304nm) photodiodes atop each sphere. Their photocurrents were measured using Keithley 6495 picoammeters. Dark measurements were obtained by blocking the light immediately before entering the reflectance sphere. The integrating spheres include baffles to prevent direct illumination of the detectors from the sample, and the ratio of the surface-coated area to the total area of the spheres (*e.g.*, the fraction not covered by input/output holes) was α=0.9652 for both spheres (which results in a sphere multiplier $M=m/(1-\alpha m)$=17.5 (774nm) and 16.7 (1304nm)).

The liquid sample cell was designed to maximize the scattering angle collected by the spheres, and consisted of two microscope slides attached to an intervening U-shaped teflon spacer of 2.0mm. Before assembly all cell surfaces were coated with Krylon Ultra-flat black paint, leaving a central window of 13mm diameter for light passage. During measurement black tape was placed over the top of the cell. After assembly the inner sample cell chamber was 2.1mm thick and outer thickness was 4.3mm. The maximum light scattering angle directly entering the spheres is limited by total internal reflection to 49° for aqueous samples. Previous experience suggests[19] that the glass slide acts to channel trapped light transversely, which may multiply interact with the sample, and which eventually enters the spheres if the sample window size is sufficiently large. For our geometry we anticipate up to 30% light loss[19] at a sample optical density τ=4, which decreases to ~2% as $\tau \to 0$. In future work the effect of this lost light might be estimated by comparing the results obtained with this absorbing cell to one constructed with a reflective coating. The refractive index of the microscope slides (Fisher) was measured using our OCT systems centered at 800nm and 1300nm to be 1.526 ± 0.004 and 1.484 ± 0.02, respectively, which allows for us to account for the cell light reflection contribution.

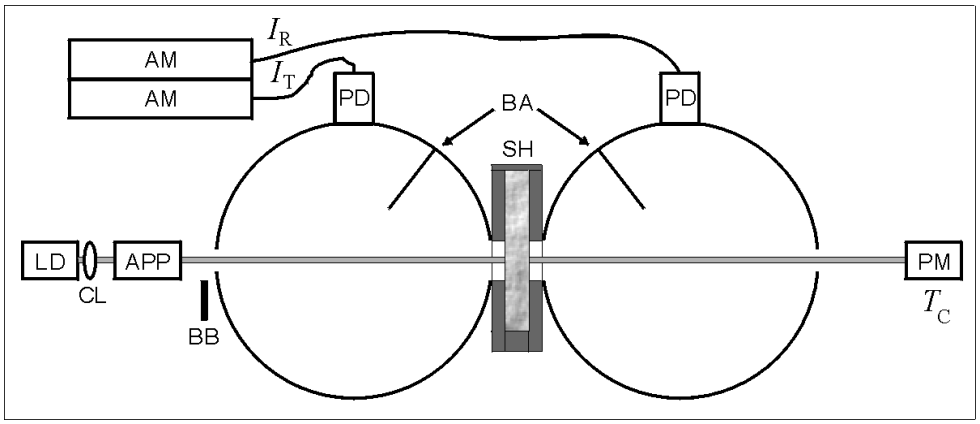

Figure 2: Diagram of double-integrating sphere system (not to scale, read text for geometry). LD=laser diode, CL=collimating lens, APP=anamorphic prism pair (774nm diode only), BB=beam blocker, PM=power meter, PD=photodiode, BA=baffle, SH=sample holder, AM=picoammeter. Measurements of I_r, I_t (reflected and transmitted photocurrent) and T_c (collimated transmission) are obtained without moving the light beam or sample.

In order to experimentally verify the reliability of μ_a and μ_s measurements with this system over the entire possible phase space, two calibration solutions, one purely scattering (albedo a ideally =1) and one purely absorbing (a ideally =0) were mixed with varying ratios and diluted to varying concentrations. Polystyrene spheres (diameter 3.3±0.04μm, BangsLabs) were employed as a high albedo calibration solution (PS stock solution). Measured values of the complex refractive index of polystyrene[9] suggest its albedo at 774 and 1304nm (via Mie theory calculations) to be 0.98 and 0.95, respectively. The μ_a and μ_s of the PS stock solution were calculated by least-squares fitting to a set of T_c measurements obtained at varying concentrations, given the predicted albedo. At 774nm, the low albedo calibration

solution was a near-infrared absorbing dye (H. W. Sands, dye #7460) in aqueous solution, filtered at 0.22μm. By assuming an albedo of 0, T_c measurements were used to predict μ_a at varying concentrations of the dye. Similarly, at 1304nm, an ink (Higgins Black Magic Waterproof Ink) was distilled into filtered water and approximated as a low-albedo solution (we used a best fit value of a=0.11). Finally, the absorption of water[20] μ_a(774nm)=0.028, μ_a(1304nm)=1.403/cm was also accounted for in predicting μ_a and μ_s of the diluted mixtures. The equations below summarize the relationship between the T_c measurements, optical density τ, sample thickness d, fractional volume f of each species i, and μ_a and μ_s for each species of albedo a present in the sample.

$$T_c = 1 - e^{-\tau} = \frac{power \quad with \quad int\,ervening \quad sample}{power \quad with \quad no \quad sample}$$
$$\tau = d\sum_i \left(\mu_{s,i} + \mu_{a,i}\right) f_i \qquad (3)$$
$$a_i = \frac{\mu_{s,i}}{\mu_{s,i} + \mu_{a,i}}; \quad \sum_i f_i = 1$$

The calibration constants b_1 and b_2 of each isolated integrating sphere[21] which account for the detector light collection efficiency were measured using a Lambertian reference sample at both wavelengths. These reference measurements were also used to normalize the double sphere measurements (as per Eq. 26, Ref. 21). Double integrating sphere measurements I_r, I_t, and T_c were then obtained for a variety of calibration solutions mixtures. These values were interpreted by an inverse-adding doubling program (IAD v.1.6 by S. Prahl) which assumes a radiative transfer model within the sample, accounts for light transport between the two integrating spheres, and computes μ_a, μ_s, and the average cosine of the scattering angle g. However, it should be noted that this model assumes unpolarized light and here we are using polarized laser light sources. Given the cylindrical symmetry of this apparatus (with the exception of the baffle), we expect that this will not be a large source of error. Initially, measurements were acquired both while blocking and unblocking the transmitted light port; however, it was determined that greater accuracy was obtained when the collimated transmitted light was allowed to leave the transmittance sphere as in Fig. 2. (We suspect this is because the large background produced by scattering this light into the transmittance sphere overwhelmed the measurement of I_t for samples with large τ). The open entrance and exit ports result in loss of light scattered at angles less than 3.5° and greater than 176.5°. We also performed the F-coefficient correction[21] for background noise reduction due to light extinction in the sample. The results of these measurements compared to the predicted values by T_c measurements are displayed in Fig. 3. Typically we observe less than 5% error, except in cases of extremely low or high albedo, where the less dominant mechanism (scattering for low albedo, absorption for high albedo) appears to be overestimated. At 1304nm, the absorption of the polystyrene spheres appears to be underestimated, which may possibly be due to less than the predicted absorption as taken from Ref. 9. The 1304nm absorption curves at low sample concentrations are dominated by the water absorption (1.403/cm). Error larger than 5% has previously been observed for samples with low albedo.[8] Since many of these errors appear to be systematic (of the same sign), possibilities for further improvements are being investigated.

Using the same procedures as for the calibration solutions, various dilutions of 10% intralipid (Liposyn II, Abbott Labs) were measured at 774 and 1304nm. The resulting μ_a and μ_s did not follow Beer's law but exhibited saturation of the extinction at higher concentrations, which is to be expected when an emulsion occupies a significant fraction of the solution volume (because it modifies the average refractive index of the medium and reduces the scattering efficiency). The three nanorods solutions described in subsection 3.1 were also measured in the same way. The results of the nanorods and intralipid measurements are reported in section 4.

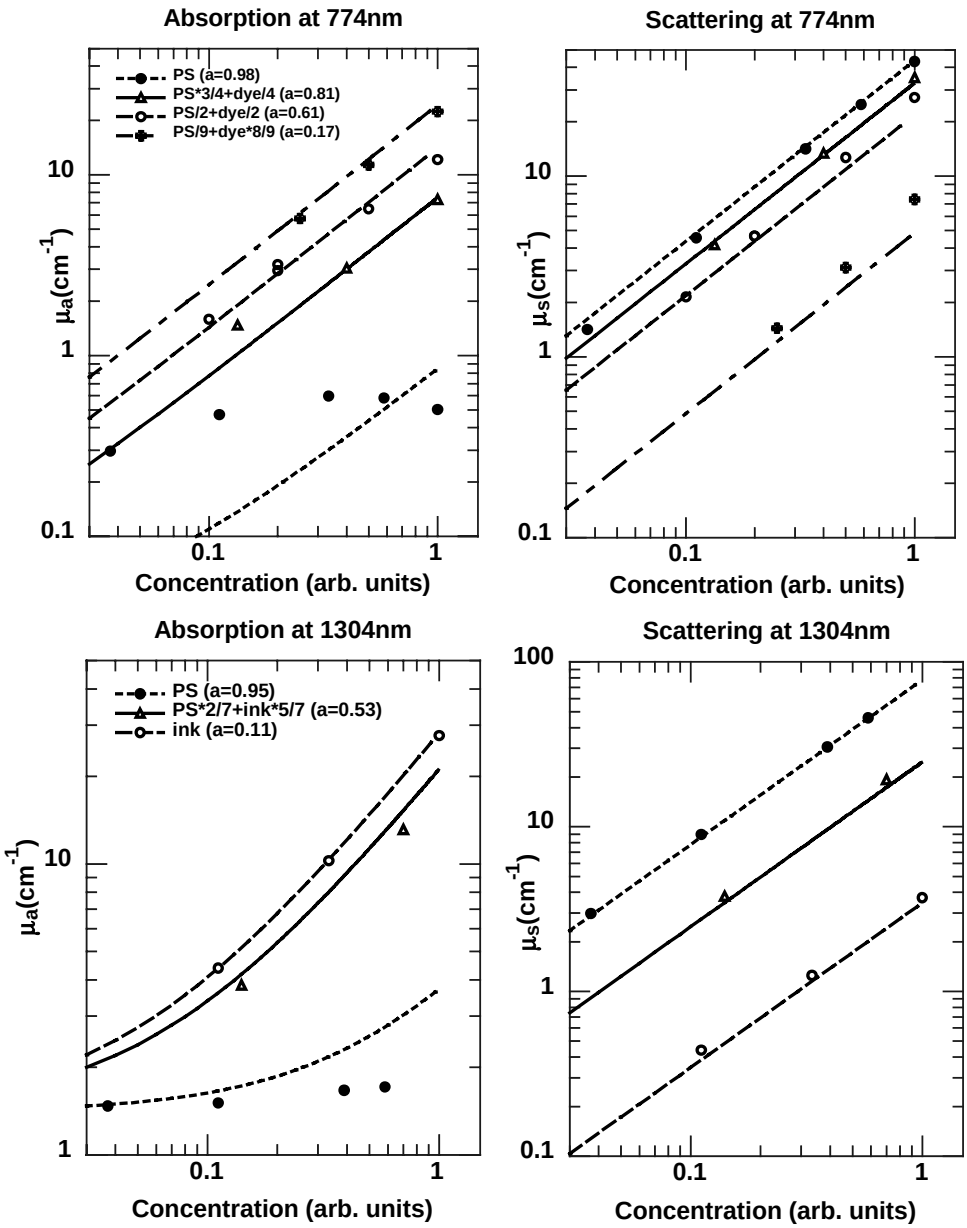

Figure 3: Plots of predicted μ_a and μ_s via T_c measurements (lines), and measured μ_a and μ_s via double-integrating spheres measurements (dots) of calibration solutions of varying albedo and optical depth, at both laser diode wavelengths. The legends describe the relative ratio of polystyrene spheres (PS), NIR absorbing dye, or ink stock solutions. Concentration is normalized such that 1 is equivalent to the full concentration of each mixture of stock solutions.

3.2 OCT Imaging System and Measurements

OCT imaging was employed to test the ability to sense an optical change while non-invasively imaging a tissue-like medium after the addition of nanorods. The OCT system employed (Fig. 4) consists of a single-mode fiber interferometer and scanning mirror optical delay, which was operated at 15 Hz. The light source was a Ti:sapphire laser (KMLabs) pumped by 5W from a 532nm Nd:YVO_4 laser (Verdi, Coherent, Inc.) The output of the Ti:sapphire laser is launched into a single-mode fiber where 10% is diverted toward the reference input of a dual-balance photodetector in order to remove noise from laser fluctuations. An optical power of 12mW was incident on the sample. The maximum sensitivity of the system was measured by imaging a mirror at the sample lens focus and placing a neutral density filter

of optical density 4 before the imaging lens (to prevent saturation of the electronics), resulting in a net power loss of 80dB after light passage in both directions. The peak signal power to noise ratio in this configuration was 21dB, resulting in a system sensitivity of 101dB. The resolution of this system is 16μm transverse (limited by the imaging lens) and 4μm axial (limited by the 100nm light bandwidth). It should be noted that an imaging lens with longer than typical focal length was chosen here to reduce the depth-dependent effect of beam focusing over the 2mm imaging depth (confocal parameter = 1.5mm).

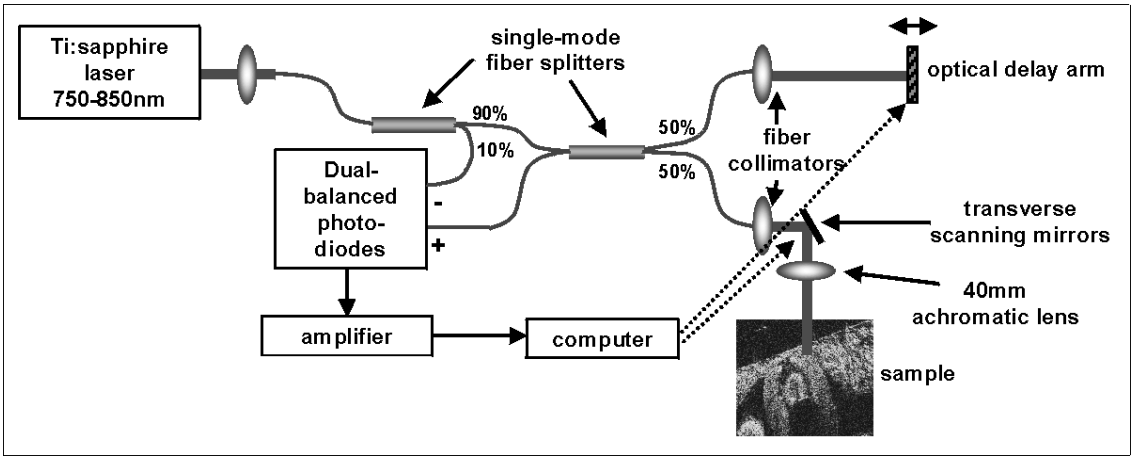

Figure 4: Diagram of the OCT system apparatus.

OCT images of varying mixtures of intralipid and nanorods solutions were acquired. Images of 2mm optical depth × 0.2mm width were acquired at 2μm/pixel. Since these are homogenous samples, the information of interest is the OCT signal (backscattered light power) as a function of depth. Therefore, the surface of the medium was placed at the same height with no tilt to reduce any error due to focusing. In this way, 100 columns were averaged to reduce random speckle fluctuations. The resulting depth-dependent backscattering profiles are reported in the following section. Note that the physical depth is reported which is the optical depth divided by n_{water}.

4. RESULTS AND DISCUSSION

A summary of the double-integrating spheres measurements of the three nanorod batches are shown in Table 1. At 774nm, the nanorod batches appear qualitatively similar in that the albedo is low (0.16-0.27) and the size of μ_a scales with the measured Au concentration. This is what one might expect given the prediction of 10% quantum efficiency for radiative decay at the resonance frequency for similar nanorods.[5] At 1304nm the absorption coefficients are generally very small after subtraction of the contribution of water, with the exception of batch #2. The apparent discrepancies between the three batches may be due to the different particle sizes. Also, batch #2 contained a higher concentration of surfactant, which may explain the larger measured value of g (the average cosine of the scattering angle) at 774nm. This difference would not be explained by the presence of 35nm spheres (g=-0.0 by Mie theory) in batch #2. Another potential source of error is additional loss of light into the sample holder due to increased side-scattering, since g is much closer to 0 than for the calibration solution of polystyrene spheres (g>0.85).

If we compare the measured μ_s/(mg/mL Au)=18 for batch #1 to that predicted by Mie theory for gold spheres (n(774nm)=0.2+4.9i),[22] we find that the value of 18/cm/(mg/mL) can only be achieved at the resonant sphere diameter of 175nm. This highlights the effectiveness of the nanorods at reducing the necessary particle size to achieve the same amount of scattering per unit Au at 774nm. Similarly, we find by Mie calculations that the absorption of gold spheres reach a maximum of μ_a/(mg/mL Au)=0.9 at a diameter of 145nm. This is significantly smaller than the measured range of 37-62/cm/(mg/mL Au) for gold nanorods. This enhancement up to 70× suggests that nanorods of the appropriate aspect ratio are particularly suited for absorption at this wavelength, and allow the use of significantly smaller volume particles.

774nm Measurements				
Nanorods batch #	μ_a (cm^{-1})	μ_s (cm^{-1})	g	μ_a(cm^{-1})/(mg/mL Au)
1	14.3	4.1	0.06	62
2	4.8	1.8	0.65	37
3	1.6	0.3	0.12	47
1304nm Measurements				(subtracted μ_a (H_2O) below)
1	1.7	0.2	0.44	1
2	3.7	3.2	0.67	17
3	2.0	0.3	0.36	16

Table 1: Optical properties of the plasmon-resonant gold nanorods measured with the double-integrating sphere system. The water μ_a of 1.403/cm at 1304nm was subtracted to evaluate the concentration-normalized absorption coefficient (right column).

Double-integrating sphere measurements of intralipid were obtained for the purposes of calibrating the OCT depth-dependent scattering profiles. The resulting extinction coefficient μ_t at 1.1% concentration was 22/cm, dominated by scattering (a=0.96). This is in agreement with previously reported values.[23]

OCT images were acquired as described previously for three concentrations of intralipid: 3.3%, 1.1%, and 0.37%. Batch #1 of the nanorods solution was mixed with each intralipid solution at concentrations of 33%, 11%, and 3.7%. Each combination was separately prepared and imaged at least twice (to account for potential microliter volume mixing errors). Also, at each intralipid concentration 3-4 control images (with no added nanorods) were acquired in between each set of nanorods images to account for potential slowly-varying laser drift. The depth-dependent scattering curves were obtained for each image by averaging across 100 columns; representative data for each mixture are displayed with their least-squares fit curve using s_0 and c as parameters (as per Eq. 2) in Fig. 5. The lens confocal parameter (1/e full width) b used in this computation was 1.5mm.

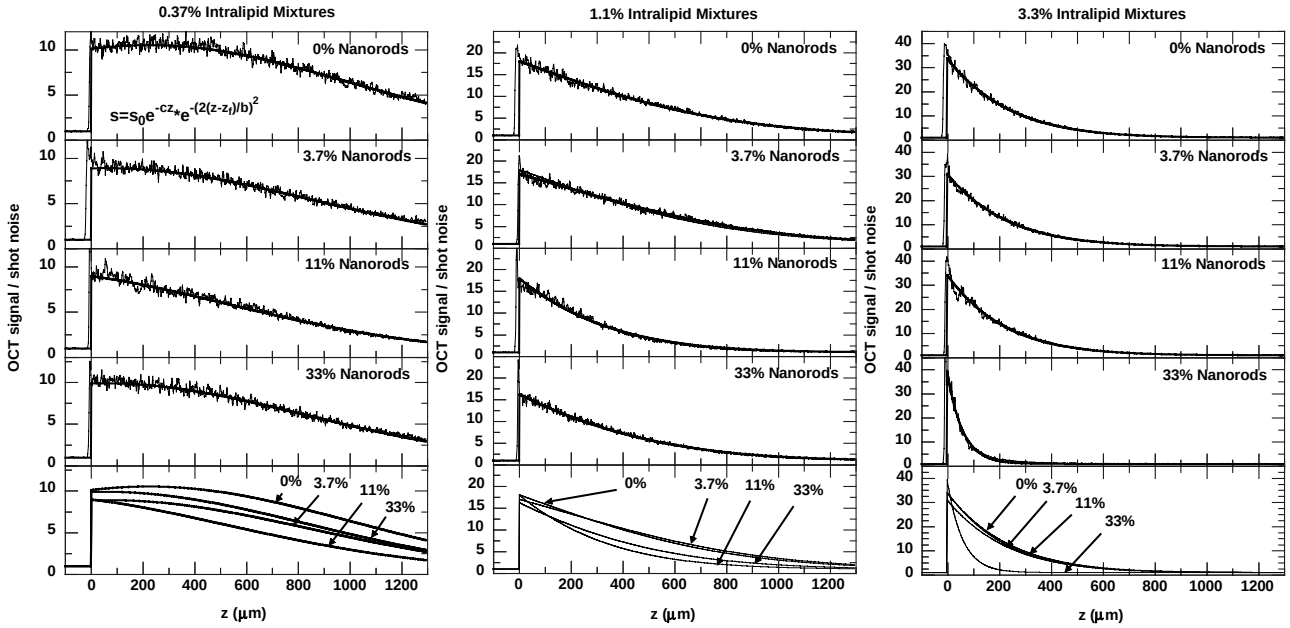

Figure 5: OCT signal s (normalized to shot noise) as a function of penetration depth z, for varying mixtures of intralipid with plasmon-resonant gold nanorods. Bold lines indicate least-squares fit of the data (narrow lines) to Eq. 2. The bottom row of graphs show comparisons of the fit curves vs. nanorods concentration.

The OCT signal depth profiles are normalized to the shot noise level at -101dB. Since 100 columns are averaged to produce this data, we expect the shot noise contribution to be 0.1 on these plots. The apparent signal-dependent noise is due to speckle noise (which is known to be approximately linearly dependent on the OCT signal s), because of insufficient spatio-temporal averaging. To properly estimate the MLR, we must have a sample-independent

measure of σ. We perform this by creating a signal-dependent profile σ(*s*) of the absolute value of the difference between the measured scattering signal and the best fit curve. (This function was found to be relatively insensitive to which images were included in the data set, so it appears to be a sample-independent factor. It was also approximately linear, as predicted by theory).

The fit parameter *c* (by Eq. 2) for each sample was used to predict the total extinction by OCT. This is compared to that predicted by T_c measurements for the pure intralipid and nanorods solutions in Table 2. (The mixtures were computed using Eq. 3). As shown, OCT is not a very accurate estimator of extinction, despite the good fit to the 2-parameter model of Eq. 2. A more advanced model of light transport relevant to OCT[24] is likely necessary to explain this discrepancy.

Concentration		Extinction Coefficient (/cm)		% difference
Intralipid	Nanorods Batch #1	by Tc	by OCT	
0.033	0.00	70	58	-18
0.033	0.037	71	55	-25
0.033	0.11	72	57	-24
0.033	0.33	76	120	45
0.011	0.00	23	22	-4
0.011	0.037	24	22	-9
0.011	0.11	25	31	21
0.011	0.33	29	36	19
0.0037	0.00	7.8	8.4	8
0.0037	0.037	8.5	12	33
0.0037	0.11	9.8	13	26
0.0037	0.33	14	15	5

Table 2: Comparison of light extinction coefficients predicted by T_c measurements and by OCT images, for each of the mixtures imaged with OCT.

The natural log of the MLR was evaluated for each image as per Eq. 1. Since several pure intralipid images were available, we arbitrarily chose one to use as the control (contrast agent-free data), and evaluated the MLR for the others as if they potentially contained nanorods. In this way, we experimentally determined a lower bound on what constitutes a significant value of MLR (one that truly indicates the presence of nanorods). The largest log MLR computed for the extra control images at each intralipid concentration is reported in Table 3. The log MLRs for each mixture (averaged over all images acquired at each mixture) are also reported here.

Taking the 0% MLR values as a baseline, we see from Table 3 that the minimum detectible concentration of nanorods approximately scales with the intralipid concentration, as one would expect. However, there is an interesting suggestion that the nanorods at 11% concentration are more easily detected than those at 33% for the lower concentrations of intralipid. This might be an aggregation effect or other surface interaction between the solutions. It may be indicative of the fact that, when the absorption becomes too great, the depth penetration is reduced and less data points are available over which to perform the statistical analysis.

Ideally one would expect the log MLR of a control image to be 0. The larger values at 0% nanorods indicate that we have underestimated our true noise, σ. This is because we did not account for fluctuations on an hour time scale due to the laser, slight displacements of the top medium surface from image to image, and liquid mixing errors. However, in a practical situation, where one has a single object, obtains a control image set, applies contrast agents, and obtains a new image set, all of these error sources can be avoided or greatly reduced. The control MLRs in such an experiment should drop significantly toward 1 and allow detection of lower concentrations of nanorods with statistical significance.

Intralipid Concentration	Nanorod Batch #1 Concentration 33%	11%	3.7%	0%
3.3%	140,000	120	170	820
1.1%	67,000	320,000	690	4,500
0.37%	10,000	110,000	27,000	1,100

Table 3: Natural log maximum likelihood ratios (MLRs) for each mixture of intralipid and nanorods (testing the hypothesis of intralipid containing nanorods vs. the hypothesis of pure intralipid). Highlighted cells indicate MLRs that are significantly larger than the maximum control at 0%, suggesting that for these concentrations of intralipid and nanorods, the nanorods can be detected with OCT.

5. CONCLUSION

The strong absorption properties of these plasmon-resonant nanorods in the near-infrared are potentially conducive to *in vivo* molecular imaging. The small particle sizes and volume concentrations of gold nanorods necessary for OCT detection are a significant improvement over spherical gold particles. Double integrating sphere measurements indicate that nanorods of nominally 15 × 45nm size exhibit an albedo of 0.16-0.27, suggesting that their primary sensing application will be absorption-based. Our MLR model is a statistically relevant quantitative measure of the ability to detect these nanorods in tissue-like media. Currently this model is limited to homogenous media. OCT images are not used to map the nanorods concentration here due to limitations in the depth scattering model. A more sophisticated model accounting for multiple scattering and dense scattering media should be developed. However, even the "yes/no" information acquired here may be useful for contrast-specific imaging. Given the large MLRs observed in this experiment, one should be able to reduce the area of interest (with a reduction in MLR) in order to map this binary information. Ultimately, biofunctionalizing the nanorods with cell receptor ligands will add molecular specificity to this technique.

ACKNOWLEDGEMENTS

We would like to acknowledge the technical contributions of Tin Man Lee, Ron Stack, Adam Zysk, and the Microanalytical Laboratory at the University of Illinois at Urbana-Champaign. This work was supported by a grant from the National Institutes of Health (1 R01 EB001777-01).

REFERENCES

1. C. H. Contag, S. D. Spilman, P. R. Contag, M. Oshiro, B. Eames, P. Dennery, D. K. Stevenson, D. A. Benaron, "Visualizing gene expression in living mammals using a bioluminescent reporter," *Photochem. Photobiol.* **66**, pp. 523-531, 1997.
2. A. Wei, "Plasmonic nanomaterials," in *Nanoparticles: Scaffolds and Building Blocks*, V. M. Rotello, Ed., Kluwer Academic, New York, pp. 173-2000, 2003.
3. S. Link, M. B. Mohamed, M. A. El-Sayed, "Simulation of the optical absorption spectra of gold nanorods as a function of their aspect ratio and the effect of the medium dielectric constant," *J. Phys. Chem. B*, **103**, pp. 3073-3077, 1999.
4. J. Yguerabide, E. E. Yguerabide, "Light-scattering submicroscopic particle as highly fluorescent analogs and their use as tracer labels in clinical and biological applications: I. Theory," *Anal. Biochem.* **262**, pp. 137-156, 1998.
5. C. Sonnichsen, T. Franzl, T. Wilk, G. von Plessen, J. Feldmann, "Drastic reduction of plasmon damping in gold nanorods," *Phys. Rev. Lett.* **88**, pp. 077402-1-3, 2002.

6. B. M. I. van der Zande, M. R. Bohmer, L. G. J. Fokkink, C. Schonenberger, "Colloidal dispersions of gold rods: synthesis and optical properties," *Langmuir*, **16**, pp. 451-458, 2000.
7. H. Kuwata, H. Tamaru, K. Esumi, K. Miyano, "Resonant light scattering from metal nanoparticles: Practical analysis beyond Rayleigh approximation," *Appl. Phys. Lett*. **83**, pp. 4625-4627, 2003.
8. S. A. Prahl, M. J. C. van Gemert, A. J. Welch, "Determining the optical properties of turbid media by using the adding-doubling method," *Appl. Opt.* **32**, pp. 559-568, 1993.
9. X. Ma, J. Q. Lu, R. S. Brock, K. M. Jacobs, P. Yang, X.-H. Hu, "Determination of complex refractive index of polystyrene microspheres from 370 to 1610 nm," *Phys. Med. Biol.* **48**, pp. 4165-4172, 2003.
10. M. Rajadhyaksha, S. Gonzalez, J. M. Zavislan, "Detectability of contrast agents for confocal reflectance imaging of skin and microcirculation," *J. Biomed. Opt.* **9**, pp. 323-331, 2004.
11. D. Levitz, L. Thrane, M. H. Frosz, P. E. Andersen, C. B. Andersen, J. Valnciunaite, J. Swartling, S. Andersson-Engels, P. R. Hansen, "Determination of optical scattering properties of highly-scattering media in optical coherence tomography images," *Opt. Express* **12**, pp. 249-259, 2004.
12. A. I. Kholodnykh, I. Y. Petrova, K. V. Larin, M. Motamedi, R, O. Esenaliev, "Precision measurement of tissue optical properties with optical coherence tomography," *Appl. Opt.* **42**, pp. 3027-3037, 2003.
13. C. Xu, D. L. Marks, M. N. Do, S. A. Boppart, "Separation of absorption and scattering profiles in spectroscopic optical coherence tomography using a least-squares algorithm," *Opt. Express* **12**, pp. 4790-4803, 2004.
14. C. Yang, M. A. Choma, L. E. Lamb, J. D. Simon, J. A. Izatt, "Protein-based molecular contrast optical coherence tomography with phytochrome as the contrast agent," *Opt. Lett*. **29**, pp. 1396-1398, 2004.
15. A. L. Oldenburg, J. R. Gunther, S. A. Boppart, "Imaging magnetically labeled cells with magnetomotive optical coherence tomography", *Opt. Lett.*, in press.
16. B. Nikoobakht, M. A. El-Sayed, "Preparation and growth mechanism of gold nanorods (NRs) using seed-mediated growth method," *Chem. Mater.* **15**, pp. 1957-1962, 2003.
17. D. A. Zweifel, A. Wei, "Sulfide-arrested growth of gold nanorods." Manuscript submitted.
18. J. W. Pickering, C. J. M. Moes, H. J. C. M. Sterenborg, S. A. Prahl, M. J. C. van Gemert, "Two integrating spheres with an intervening scattering sample," *JOSA A* **9**, pp. 621-631, 1992.
19. S. Prahl, "Optical property measurements using the inverse adding-doubling program", published online at http://omlc.ogi.edu/software/iad/manual/, Ch. 6, pp. 29-34, January, 1999.
20. L. Kou, D. Labrie, P. Chylek, "Refractive indices of water and ice in the 0.65-2.5μm spectral range," *Appl. Opt.* **32**, pp. 3531-3540, 1993.
21. J. W. Pickering, S. A. Prahl, N. van Wieringer, J. F. Beek, H. J. C. M. Sterenborg, M. J. C. van Gemert, "Double-integrating-sphere system for measuring the optical properties of tissue," *Appl. Opt.* **32**, pp. 399-410, 1993.
22. E. D. Palik, ed., *Handbook of Optical Constants of Solids II*, Academic Press, Boston, 1991.
23. A. Giusto, R. Saija, M. A. Iati, P. Denti, F. Borghese, O. I. Sindoni, "Optical properteis of high-density dispersions of particles: application to intralipid solutions," *Appl. Opt.* **42**, pp. 4375-4380, 2003.
24. P. E. Andersen, L. Thrane, H. T. Yura, A. Tycho, T. M. Jorgensen, M. H. Frosz, "Advanced modelling of optical coherence tomography systems," *Phys. Med. Sci. Biol.* **49**, pp. 1307-1327, 2004.